

Effective interactions mediated between two permeable disks in an active fluid

Mahmoud Sebtosheikh* and Ali Naji†

School of Physics, Institute for Research in Fundamental Sciences (IPM), P.O. Box 19395-5531, Tehran, Iran

We investigate the behavior of self-propelled active Brownian particles (ABPs) in an active bath involving two permeable disklike inclusions, whose interior and exterior regions are characterized by mismatching motility strengths (Péclet numbers) for the active particles. We show that the inhomogeneous motility field strongly affects the spatial distribution of the ABPs and the effective forces imparted on the inclusions as the ABPs interact with and/or pass through their enclosing membranes. These forces emerge as a result of the anisotropic distribution of ABPs in the presence of the two inclusions and, as such, represent effective bath-mediated interactions between them. We show that these forces are repulsive when the interior and/or exterior Péclet numbers are sufficiently small and the ABPs are either mainly saturated within or depleted from the inclusions. Attractive forces emerge in a wide range of intermediate values of Péclet numbers. While the repulsive interactions arise because of the dominant forces imparted on the inclusions from the exterior ABPs as they acquire increased concentrations in the intervening gap between the inclusions, the attractive interactions are found to have a more subtle origin in the forces exerted on the enclosing membranes from the interior ABPs. We elucidate these mechanisms and present an overall phase diagram summarizing the regimes of repulsion/attraction for varying interior/exterior Péclet numbers.

I. INTRODUCTION

Effective interactions between colloidal inclusions suspended in bathing aqueous solutions is of crucial importance in predicting phase behaviors of colloidal suspensions and in manipulating them for numerous technological applications [1–3]. Depletion forces are one of the primary types of effective interactions that emerge in size-asymmetric suspensions, consisting of colloidal inclusions and smaller-sized depletant particles such as short polymers [4, 5]. The depletion force is typically short-ranged, *attractive* and of entropic origin, arising from the steric exclusion of depletants from the proximity of inclusions.

Even though depletion forces are thoroughly investigated in mixtures of passive Brownian particles [1], their nonequilibrium counterparts, especially in the newly emerging context of active Brownian particles (ABPs) [6–13], have been investigated only over the last few years [14–26]. It was shown that, unlike the passive case, active depletants cause *repulsive* interactions between two hard disklike inclusions immersed in the bath [14], with the interaction profile later shown to consist of distinct peaks caused by ABP layering or ring formation around the inclusions at well-separated radial distances [15].

These nonequilibrium effective forces have been investigated in various cases to elucidate their dependence on the geometric shape of the inclusions [14, 21, 23, 25], the depletant/inclusion size ratio [14, 17, 20, 21, 23], interparticle interactions [17] and on the concentration [17, 21, 23] and chirality of ABPs [15]. While most of these studies focused on two-body interactions between suspended inclusions, the three-body interactions [15] and bulk properties, such as cluster formation and phase separation,

in many-particle systems involving ABPs and colloidal spheres [26] have also been explored. In contrast to passive particles, ABPs strongly accumulate near confining boundaries due to their persistent self-propulsive motion [27–32]. Because of their excluded-volume interactions, ABPs produce high-density layers at and oscillating force profiles between juxtaposed hard boundaries [14, 15, 17, 19, 20, 23, 24]. The ABP layering varies depending on the shape of the inclusions and density of ABPs. Thus, in the case of plane-parallel surfaces (or parallel rectangular inclusions) at a relatively high density of active bath, where the surface accumulation of ABPs is stronger relative to the case of disklike inclusions, the layering effects are relatively stronger and the bath-mediated forces are repulsive and more strongly oscillating as well [17]. By decreasing density of the active bath, the range of the repulsive part of the force profile, which appears at sufficiently small separations between the inclusions, is shortened, and a long attractive tail emerges; the latter being due to the fact that the ABP layering in the extended gap between the rectangular inclusions is weaker than the one occurring on the far side of the inclusions [14, 17]. In shaken granular beds with inclusions modeled as dimers, when the direction of shaking is not parallel or perpendicular to the axis of the dimer, effective interactions between the inclusions is found to be noncentral [24].

In this work, we consider the problem of effective interactions mediated between two fixed *permeable* inclusions immersed in an active bath of ABPs described within a customarily used two-dimensional model. The interior and exterior regions of the inclusions are assumed to produce different self-propulsion strengths for ABPs, enabling us, in particular, to explore the role of the motility field inhomogeneity in the system. Self-propelled particles in environments with heterogeneous motility fields have previously been considered in a number of works [33–41]. The ABPs concentrate more strongly in regions

* mahmoud-sebtosheikh@ipm.ir (corresponding author)

† a.naji@ipm.ir

of lower motility strength as they exhibit relatively longer persistence times over those regions. As a result, ordered states such as crystal and liquid crystalline phases of ABPs have been found in media with lower motility strengths [35, 37], while self-assembled structures such as membranes of self-propelled rods have been found to form spontaneously at the interface of two media with mismatching motility strengths [37].

We investigate how the inclusion permeability and the presence of a heterogeneous motility field affect the effective forces acting on the inclusions. While by increasing the motility of ABPs in an active bath containing two hard (impermeable) inclusions, one finds stronger repulsive forces, the effective interactions turn out to have a more complex dependence on the exterior/interior motility strengths (Péclet numbers) of ABPs, when the inclusions are permeable. For instance, repulsive interactions are found typically when ABPs are either predominantly depleted from or saturated within the interior regions of the inclusions, while attractive interactions emerge in a wide region across the parameter space, where the exterior/interior motility strengths are comparable.

The paper is organized as follows. In Section II, we introduce our model and simulation methods. The typical distribution of ABPs inside and outside the inclusions is discussed in Section III, followed by a detailed analysis of the effective forces exerted on the inclusions in Section IV. The paper is concluded in Section V.

II. MODEL AND METHODS

We consider a minimal model of dislike active Brownian particles (ABPs) with fixed self-propulsion speeds and diameter σ in two dimensions [42]. The ABPs are dispersed in a base fluid, which includes two fixed disk-shaped fluid enclosures, or inclusions, with effective diameter $\sigma_c + w$. The bounding enclosures are characterized by a soft, repulsive, steric potential (to be specified later) and, as such, model permeable interfacial regions, or membranes, of thickness $w = \sigma$ enclosing the inclusions; see Fig. 1. Examples of such micro-compartments may include vesicles, lipid domains [43–45], immiscible or stabilized droplets in emulsions, or the recently studied realizations of active droplets [46–48]. The surface-to-surface distance of the two inclusions is denoted by d .

The ABPs exhibit different self-propulsion speeds, v_c and v_m , inside and outside the inclusions, respectively, presenting a case of discontinuous motility field [35, 37], formally expressed as

$$v(\mathbf{r}) = v_c + (v_m - v_c) \sum_{k=1,2} \Theta(|\mathbf{r} - \mathbf{R}_k| - \sigma_c/2), \quad (1)$$

where $\mathbf{r} = (x, y)$ denotes the spatial coordinates, \mathbf{R}_1 and \mathbf{R}_2 denote the position vectors of the inclusion centers, and $\Theta(\cdot)$ the Heaviside step function.

The overdamped Brownian dynamics of ABPs (labeled

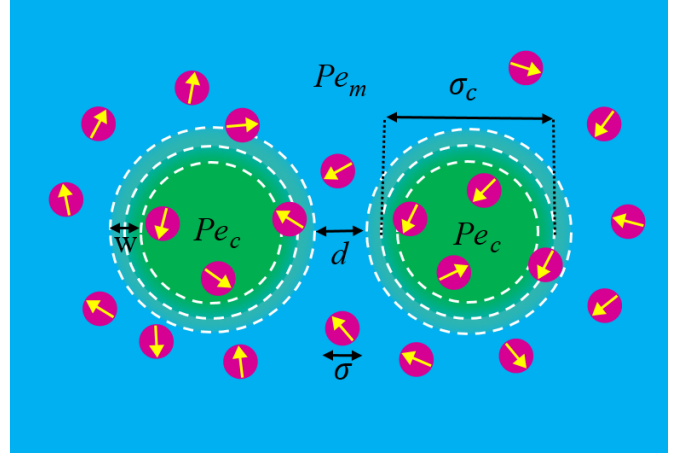


Figure 1. Schematic view of two fixed permeable inclusions in a bath of active Brownian particles that attain mismatching motility strengths, or Péclet numbers, Pe_c and Pe_m , in the interior and exterior regions of the inclusions, respectively.

by $i = 1 \dots, N$) are governed the Langevin equations,

$$\dot{\mathbf{r}}_i = v(\mathbf{r}_i) \mathbf{n}_i - \mu_T \frac{\partial U}{\partial \mathbf{r}_i} + \eta_i(t), \quad (2)$$

$$\dot{\theta}_i = \zeta_i(t), \quad (3)$$

where $\{\mathbf{r}_i(t)\} = \{(x_i(t), y_i(t))\}$ are the position vectors and $\{\mathbf{n}_i(t)\} = \{(\cos \theta_i(t), \sin \theta_i(t))\}$ are the self-propulsion orientation vectors of ABPs. The angular orientation θ_i is measured from the x -axis. Also, μ_T is the translational mobility, $U = U(\{\mathbf{r}_j\}, \{\mathbf{R}_k\})$ is the sum of the interaction potentials between the constituent particles (see below), and $\eta_i(t)$ and $\zeta_i(t)$ are the translational and rotational noises, respectively. These are assumed to be white, Gaussian-distributed noises of thermal origin, with zero mean, $\langle \eta_i(t) \rangle = \langle \zeta_i(t) \rangle = 0$, and the correlators

$$\langle \eta_i(t) \eta_j(t') \rangle = 2D_T \delta_{ij} \delta(t' - t) \quad (4)$$

$$\langle \zeta_i(t) \zeta_j(t') \rangle = 2D_R \delta_{ij} \delta(t' - t), \quad (5)$$

where D_T and D_R are the translational and rotational diffusivities, respectively. The Einstein-Smoluchowski-Sutherland relation implies $D_T = \mu_T k_B T$, and the low-Reynold-number (Stokes) hydrodynamics for no-slip spheres implies $D_R = 3D_T/\sigma^2$ [49].

The ABPs are assumed to interact with each other via a Weeks-Chandler-Andersen (WCA) pair potential, U_{WCA} ; i.e., for the i th and j th ABPs, we have

$$U_{\text{WCA}}^{(ij)} = \begin{cases} 4\epsilon \left[\left(\frac{\sigma}{r_{ij}} \right)^{12} - \left(\frac{\sigma}{r_{ij}} \right)^6 + \frac{1}{4} \right] & : r_{ij} \leq 2^{1/6} \sigma, \\ 0 & : r_{ij} > 2^{1/6} \sigma, \end{cases} \quad (6)$$

where $r_{ij} = |\mathbf{r}_i - \mathbf{r}_j|$. Also, as they go through the interfacial regions (membranes) of the inclusions, the ABPs are assumed to experience a soft repulsive WCA (sWCA)

potential [50]. For the ensuing interfacial interaction of the i th ABP with the k th inclusion, we use

$$U_{\text{sWCA}}^{(ik)} = \begin{cases} 4\epsilon' \left[\left(\frac{\sigma'}{\sqrt{r_{ik}^2 + \alpha^2}} \right)^{12} - \left(\frac{\sigma'}{\sqrt{r_{ik}^2 + \alpha^2}} \right)^6 \right] + U_0 & : r_{ik}' \leq \sigma', \\ 0 & : r_{ik}' > \sigma', \end{cases} \quad (7)$$

where $r_{ik}' = |\mathbf{r}_i - \mathbf{R}_k| - \sigma_c/2$ and

$$U_0 = -4\epsilon' \left[\left(\frac{1}{1 + (\alpha/\sigma')^2} \right)^6 - \left(\frac{1}{1 + (\alpha/\sigma')^2} \right)^3 \right], \quad (8)$$

$$\sigma' = (\sigma + w)/2, \quad \alpha = \sigma'(2^{1/3} - 1)^{1/2} \sigma',$$

and we use representative values of $\epsilon = 10k_B T$ and $\epsilon' = 0.0127k_B T$. The sWCA potential is regularized by the term α^2 appearing in the denominators, enabling permeation of ABPs of sufficiently large momenta across the potential barrier set by the enclosing membranes.

We study the steady-state properties of the system by solving the aforementioned Langevin equations using a discrete time step δt . A dimensionless representation is obtained by rescaling the space and time coordinates using $\tilde{x} = x/\sigma$, $\tilde{y} = y/\sigma$ and $\tilde{t} = tD_T/\sigma^2$, giving

$$\tilde{x}_i(\tilde{t} + \delta\tilde{t}) = \tilde{x}_i(\tilde{t}) + (2Pe \cos \theta_i + \tilde{f}_{x,i})\delta\tilde{t} + \sqrt{2\delta\tilde{t}} R_{x,i} \quad (9)$$

$$\tilde{y}_i(\tilde{t} + \delta\tilde{t}) = \tilde{y}_i(\tilde{t}) + (2Pe \sin \theta_i + \tilde{f}_{y,i})\delta\tilde{t} + \sqrt{2\delta\tilde{t}} R_{y,i} \quad (10)$$

$$\theta_i(\tilde{t} + \delta\tilde{t}) = \theta_i(\tilde{t}) + \sqrt{2\chi\delta\tilde{t}} R_{\theta,i}, \quad (11)$$

where

$$\tilde{f}_{x,i} = -\frac{\partial \tilde{U}}{\partial \tilde{x}_i}, \quad \tilde{f}_{y,i} = -\frac{\partial \tilde{U}}{\partial \tilde{y}_i} \quad (12)$$

are the rescaled force components acting on the i th ABP and $\tilde{U} = U/k_B T$. Also, $R_{x,i}$, $R_{y,i}$, and $R_{\theta,i}$ are independent Gaussian random numbers with zero mean and unit variance, and we have $\chi = \sigma^2 D_R/D_T = 3$. Here, $Pe = \{Pe_c, Pe_m\}$ is the Péclet number, defined as

$$Pe_{c,m} = \frac{\sigma v_{c,m}}{2D_T} \quad (13)$$

for the interior (c) and exterior (m) regions.

In our simulations, we fix the area fraction of ABPs, $\phi = N\pi\sigma^2/(4L_x L_y)$, and that of the inclusions, $\phi_c = \pi\sigma_c^2/(2L_x L_y)$, at distinct values of $\phi = \{0.2, 0.4\}$ and $\phi_c = \{0.05, 0.025\}$. Here, L_x and L_y give the lateral dimensions of the bounding simulation box that is used with periodic boundary conditions to mimic the bulk conditions; in all cases, we take a square box $L_x = L_y$, except the case with $\phi_c = 0.025$ (last figure), where we use a rectangular one with $L_x = 2L_y$ to capture the full range of the interaction force without the undesired boundary effects. As defined, ϕ gives the nominal area fraction

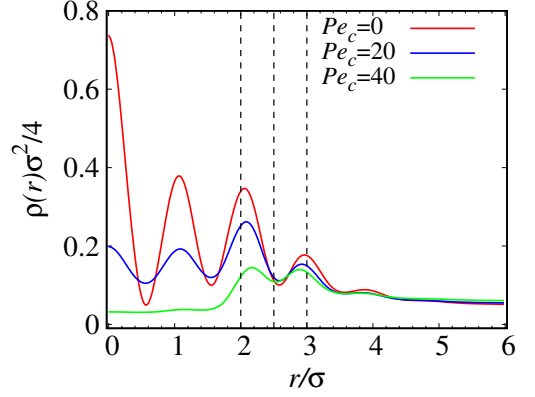


Figure 2. Rescaled radial density profiles of ABPs are shown as a function of the rescaled radial distance from the center of an *isolated* inclusion for $Pe_c = 0, 20, 40$ at fixed $Pe_m = 40$.

of a homogeneous bulk with no inclusions present. Because of strong boundary effects due to the inclusions in the present setting, the motility-induced phase separation [51] that may otherwise occur in an equivalent bulk system is strongly suppressed. The interior regions are dominated by ringlike structures when populated by ABPs (see below) and the exterior regions, whose area fraction at most reaches values in the range 0.16-0.2, can only exhibit small ABP clusters of no significant effect on the forces acting on the inclusions.

The diameter of the inclusions is taken as $\sigma_c = 5\sigma$ and 10σ with the simulation box size taken for these cases as $L = 28\sigma$ and 56σ , respectively, while the area fraction is kept fixed. The interior/exterior Péclet numbers is varied over a wide range of values from zero up to 200.

The simulations are run using 200 up to 800 ABPs with a simulation time step of $\delta\tilde{t} = 1.33 \times 10^{-5}$. We use $(2 - 6) \times 10^7$ total simulation time steps with the first 10^7 steps used for relaxation purposes. The averages are performed over a sample of 3 up to 20 independent simulations, with the larger number of samples typically used for the larger area fractions.

III. SPATIAL DISTRIBUTION OF ABPS

When the disklike inclusions are located at large distances from one another (e.g., $d/\sigma = 8$), the spatial distribution of ABPs around them exhibits spherical symmetry both inside and outside the inclusions. Figure 2 shows the radial number density, $\rho(r)$, of ABPs as a function of the radial distance, r , from the center of one of the disks (with the results being independent of the choice of the inclusion). In the case where particle motility vanishes inside the inclusions, $Pe_c = 0$ (nonactive interior; red solid curve), there is a larger concentration of ABPs inside the inclusions relative to the cases with $Pe_c > 0$ (blue and green solid curves). This is in accord with previous findings in inhomogeneous systems [33–35], in-

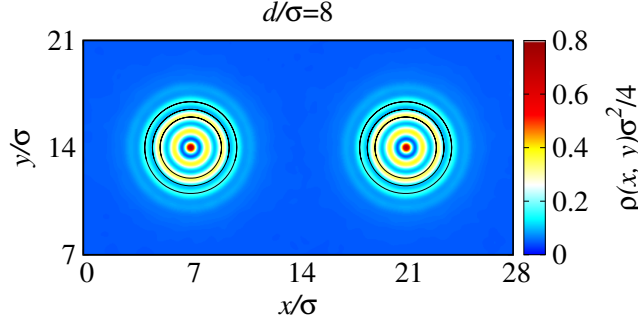


Figure 3. Color-coded density maps of ABPs for two isolated inclusions for $Pe_c = 0$, $Pe_m = 40$, $\phi = 0.2$ and $\phi_c = 0.05$. Red/yellow colors indicate regions of high/intermediate particle density, while cyan/blue indicate regions of reduced/nearly vanishing particle density. The interfacial region for each inclusion is shown by three black solid circles (see also Fig. 1).

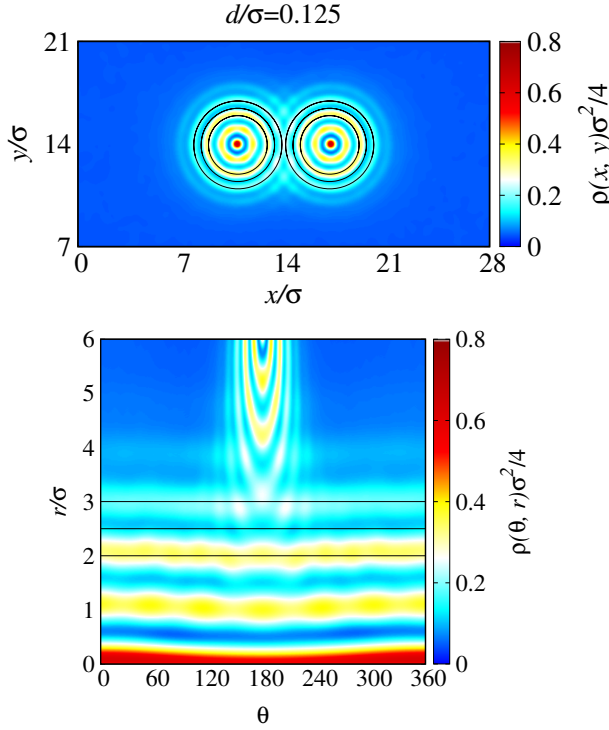


Figure 4. Color-coded density maps of ABPs for two inclusions for $d = 0.125$, $Pe_c = 0$, $Pe_m = 40$, $\phi = 0.2$ and $\phi_c = 0.05$. Top and bottom panels show distribution of ABPs in Cartesian and polar coordinates, respectively. The interfacial region for each inclusion is indicated by three black solid circles (lines) in the top (bottom) panel, respectively.

indicating that the steady-state particle density varies with the inverse-square-root of the effective diffusion constant, or approximately that of the Péclet number, when the Péclet number is sufficiently large. The density profiles of Fig. 2 display oscillatory behaviors, mirroring the ring-

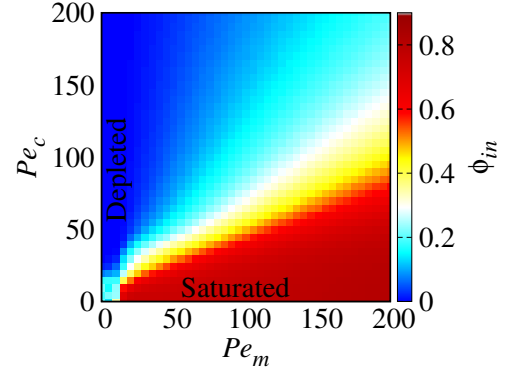


Figure 5. Internal area fraction of ABPs within the permeable inclusions as a function of Pe_c and Pe_m for $\phi = 0.2$ and $\phi_c = 0.05$, when the inclusions are at contact, $d = 0$.

like structures of high and low particle-density regions inside the inclusions, as depicted in the color-coded density maps of Fig. 3 for $Pe_c = 0$ and $Pe_m = 40$. These circular structures arise from the excluded-volume repulsions between the particles [14, 15]. As Pe_c is increased, ABPs at the central regions inside the inclusions are more strongly depleted than those near the interfacial regions ($2 \leq r/\sigma \leq 3$). This reflects the slow-down of ABPs near the interfacial regions by the enclosing membrane potential. Evidently, as Pe_c is further increased (green curve), ABPs almost completely vacate the interior regions, while, in all cases, the exterior particle density is only weakly influenced by the changes in Pe_c .

The radial symmetry of the ABP distribution is broken when the two inclusions are placed nearby. This is shown in Fig. 4a, where multiple intersections between individual rings formed around each inclusion are illustrated (they are discerned more clearly in the closeup view in Fig. 4b). It is this asymmetric distribution of ABPs in and around the inclusions that causes an effective interaction force between them, which we shall explore in the following section. The outside ABPs are more strongly accumulated in the intervening wedge-shaped gap between the inclusions and the inside ABPs are more strongly accumulated in the farther extremities of the interior regions, causing an effective force on the enclosing membranes of the inclusions that is of repulsive nature.

Before proceeding further, we briefly examine the *internal* area fraction of ABPs within the inclusions as a function of Pe_c and Pe_m ; see Fig. 5. Being defined as $\phi_{in} = N_{in}\sigma^2/(2\sigma_c^2)$, where N_{in} is the number of particles trapped inside both inclusions, ϕ_{in} increases by increasing Pe_m or decreasing Pe_c , which, as noted before, is due to the relatively longer times ABPs spend inside the inclusions. However, ϕ_{in} cannot exceed a certain value due to steric repulsions between ABPs [35, 38], leading to a finite saturation level (dark red colors in the figure).

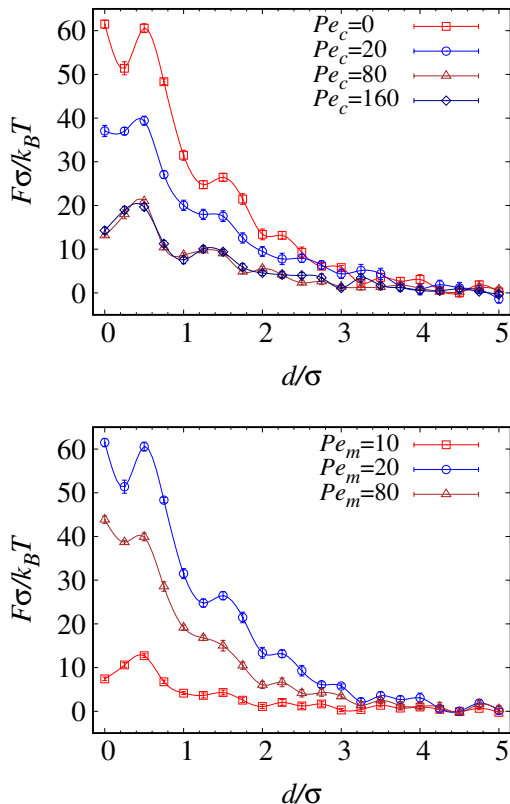


Figure 6. Effective force acting on the inclusions as a function of their rescaled surface-to-surface distance, d/σ , for fixed $Pe_m = 20$ and different values of Pe_c (top) and for fixed $Pe_c = 0$ and different values of Pe_m (bottom), as indicated on the graph. In both panels, $\phi = 0.2$ and $\phi_c = 0.05$.

IV. EFFECTIVE INTERACTIONS

A. Force-distance profiles

The rescaled effective force acting on the inclusions due to their direct interactions with the spatially dispersed active particles around them can be obtained using

$$F(d)\sigma/k_B T = - \sum_i \langle \tilde{f}_{x,i} \rangle, \quad (14)$$

where $-\langle \tilde{f}_{x,i} \rangle$ is the x -component (along the center-to-center axis of the inclusions) of the mean force imparted on the enclosing membrane as it comes into contact with the i th ABP; see Eq. (12). The summation in Eq. (14) is computed only for ABP-membrane interactions associated with one of the inclusions since, by the left-right symmetry of the system (Fig. 1), the mean force calculated by choosing either of the inclusions is found to be nearly the same within the simulation errors. Likewise, because of up-down symmetry of the system, the y -component of the force averages out to zero.

Figure 6 (top) shows the effective force between the permeable inclusions as a function of their surface-to-

surface distance, d , at fixed exterior Péclet number, $Pe_m = 20$, and for the interior Péclet number increased from $Pe_c = 0$ up to $Pe_c = 160$. As a general trend, the force profiles indicate repulsive interactions with a characteristic oscillatory behavior, exhibiting a number of successive local maxima and minima, as the overall magnitude of the force decreases with d . These local minima and maxima can be understood directly based on the overlaps between the rings of ABPs that form around each of the inclusions (and also the intersections of the rings associated with one inclusion with the bounding surface of the other inclusion) as d is varied. These mechanisms have been elucidated in detail in Ref. [15] and we shall not delve further into discussing them here. As seen in Figure 6 (bottom), a similar behavior is found for the effective force, when the interior Péclet number, Pe_c , is kept fixed (here, $Pe_c = 0$) and Pe_m is varied. The dependence of the force profiles in the two above-mentioned cases, however, turns out to be distinctly different, as we shall explore next.

B. Role of exterior/interior motility strengths

Our data in Fig. 6 show that, as the interior Péclet number, Pe_c , is increased at fixed exterior Péclet number, Pe_m , the magnitude of the force acting on the inclusions decreases, converging to a limiting curve already for $Pe_c = 80$. This behavior is illustrated in Fig. 7 (top), where we concentrate on the contact force $F_0 = F(d=0)$ as a function of Pe_c at different fixed values of Pe_m . The interaction force on the inclusions drops smoothly as Pe_c increases. When Pe_m is small (see, e.g., the data with $Pe_m = 25$ in Fig. 7, or $Pe_m = 20$ in Fig. 6, top), the force decreases monotonically and tends to a nonvanishing constant as Pe_c is increased. When Pe_m is sufficiently large (e.g., $Pe_m = 50$), the force behavior with Pe_c exhibits a weak and broad maximum before it drops to zero. This behavior can be understood as follows.

The effective force acting on the inclusions can be viewed as a resultant effect of two separate force components imparted by interior and exterior ABPs on the enclosing membrane of the inclusions, to be referred to as internal and external forces, respectively. To understand the dependence of the effective force on particle motility, one needs to understand how these force components vary with the Péclet numbers. The force components are directly influenced by the concentration of ABPs accumulated near the boundary regions of the inclusions and, specifically, also within their interior regions.

We first consider how the internal ABP concentration changes with Pe_c at fixed Pe_m . It turns out that the internal ABP concentration decreases as Pe_c is increased and that the rate of this decrease varies inversely with Pe_m ; see Fig. 5. At high Pe_m , internal concentration remains constant then decreases as Pe_c is increased. When Pe_c is below a certain threshold, internal concentration is found to be in the saturated regime.

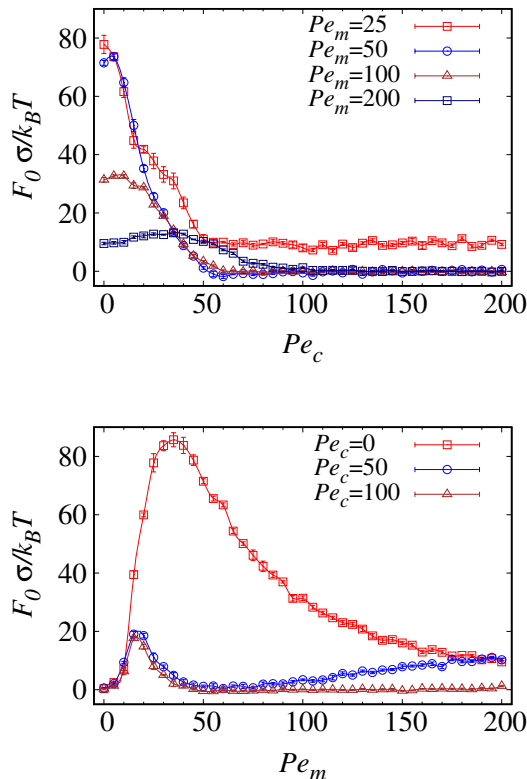


Figure 7. Contact force, $F_0 = F(d = 0)$, acting on the inclusions as a function of Pe_c for different fixed values of Pe_m (top) and as a function of Pe_m for different fixed values of Pe_c (bottom), as indicated on the graphs. In both panels, $\phi = 0.2$ and $\phi_c = 0.05$.

In the cases where Pe_m is fixed (Fig. 7, top), the external force depends only on the effective hardness of the inclusions and is directly related to the internal ABP concentration. It is nevertheless important to note that in addition to the hardness produced by the enclosing membrane, external ABPs also encounter resistance from internal ABPs accumulated within the inclusions. At different values of fixed Pe_m , by increasing Pe_c , external force monotonically decreases down to a constant value. This is because, when the interior regions are nearly fully depleted from ABPs, effective hardness of the inclusions reduces to that of the enclosing membranes. By increasing Pe_c , the internal force does not remain constant. The internal force depends on the momenta and the concentration of internal ABP and, as such, varies proportionally with these quantities. At low Pe_m such as $Pe_m = 25$, the internal ABP concentration rapidly decreases and, hence, the internal force monotonically decreases. At high Pe_m such as $Pe_m = 200$, however, as Pe_c is initially increased, the internal ABP concentration remains constant then decreases slowly; hence, the internal force increases up to a maximum, because of the constant ABP concentration and increase in ABP momenta, but after

that, it decreases because of the decrease in ABP concentration.

We now turn to the case, where the exterior Péclet number, Pe_m , is varied at fixed interior Péclet number, Pe_c . Figure 6 (bottom) reveals that, in this case, the force profile depends on Pe_m in a nonmonotonic fashion (compare the data for $Pe_m = 20$ with the two other data sets). This behavior is more thoroughly shown for the contact force as a function of Pe_m at different fixed values of Pe_c in Fig. 7 (bottom). The force indeed increases up to an intermediate value of Pe_m^* , where it takes a pronounced global maximum. For $Pe_c = 0$, we find $Pe_m^* \simeq 35$, a value that becomes significantly smaller, when Pe_c is fixed at larger values, as shown the figure.

In the cases where Pe_c is kept fixed (Fig. 7, bottom), there are several factors that control (e.g., enhance or suppress) the effective force imparted on the inclusions. By increasing Pe_m , the ABPs present in the exterior regions impart stronger ‘kicks’ on the enclosing membranes as they come in contact with the latter. The internal concentration of ABPs increases and this is the factor that enhances the effective force. On the other hand, by increasing Pe_m , the average time of interaction between external ABPs and the enclosing membranes decreases and also the ringlike structures of ABPs outside and inside the inclusions are weakened, as the exterior ABPs become more strongly motile and produce stronger kicks with the interior ABPs. These latter factors are the ones that suppress the effective force produced on the inclusions. The exact contribution due to each of these factors cannot be determined as they are inter-related and they are not expected to contribute linearly to the effective force. At fixed $Pe_c = 0$, an initial increase in Pe_m gives a dominant increase in the momenta of external ABPs and their internal concentration, and thus an increase in the effective force, but these factor are eventually overtaken by the factors that create effective force suppression. At fixed $Pe_c = 50$, by increasing Pe_m in the range $[0, 50]$, where the internal concentration is diluted (see Fig. 5), there appears to be a competition between the increase in the momenta of external ABPs and the decrease in the average time of the interaction between external ABPs and the enclosing membranes. As Pe_m is increased, the former factor becomes dominant and, as a result, the effective force increases but, on further increase of Pe_m , the latter factor dominates and, hence, the effective force decreases. In the range $Pe_m > 50$, the internal ABP concentration increases with Pe_m ; this, being the dominant factor in this regime of parameters, causes an increase in both internal and external forces and, as a result, an increase in the effective force. The increase in the effective force continues until a secondary hump appears, as seen in Fig. 7 (blue curve). The said increase stops after the internal concentration is saturated, in which case, the decrease in the interaction time becomes dominant again and, thus, the effective force decreases. At $Pe_c = 100$, the same mechanisms hold except that the second hump does not appear in the range $Pe_m < 200$, because the

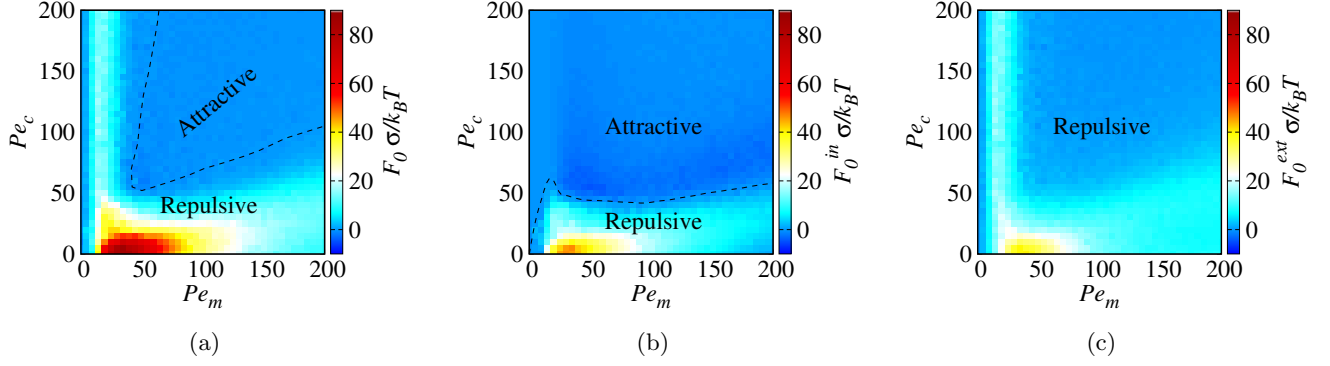


Figure 8. (a) The net effective force acting on the inclusions at contact plotted along with (b) the internal force and (c) the external force components as functions of Péclet numbers Pe_c and Pe_m for $\sigma_c = 5$, $\phi = 0.2$ and $\phi_c = 0.05$. The dashed curves in (a) and (b) show the borders between repulsive and attractive force regimes.

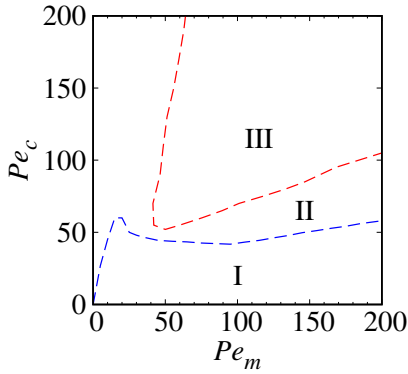


Figure 9. Borders of different parametric regions I-III corresponding to the plots in Fig. 8. These regions are determined based on the ABP distribution and the force components as discussed in the text.

internal concentration only weakly increases with Pe_m .

C. Regimes of attraction and repulsion

Even though our focus in the preceding sections has mainly been on the regime of parameters, where the forces acting on the inclusions are found to be repulsive (positive), there are other regimes, where the forces turn out to be attractive (negative) and would thus tend to bring the inclusions closer together. We run extensive simulations across a wide range of values over the (Pe_m, Pe_c) plane to evaluate the magnitude and the sign of the net effective force acting on the inclusions and their internal and external components. The results are shown for the net force F_0 acting on the inclusions at contact, its internal component F_0^{in} and its external component F_0^{ext} , fulfilling the relation $F_0 = F_0^{in} + F_0^{ext}$, as color-coded density maps in Fig. 8a, b and c, respectively. As seen in panel a, the net force is repulsive for sufficiently

small Pe_m and/or Pe_c , with a maximal value (red spot) obtained for Pe_c , i.e., when the interior Péclet number is zero and $Pe_m^* \simeq 35$. The net force becomes attractive in the central (triangular) region of the parameter space enclosed by the dashed curve. The figure indicates a minimum value of $Pe_c \simeq 50$ and $Pe_m \simeq 40$ below which attraction is not possible.

Panels b and c show that a net attraction originates in the internal component, F_0^{in} , of the force acting on the inclusions, as F_0^{ext} never becomes attractive. Panel b also indicates that F_0^{in} becomes attractive typically when $Pe_c \gtrsim 50$, unless Pe_m tends to zero, in which case the threshold Pe_c (above which F_0^{in} becomes attractive) also tends to zero.

Further insight can be obtained by comparing the regions of attraction and repulsion in Figs. 8a-c with the regions of the parameter space, where ABPs are found to be depleted from or saturated within the inclusions; see Fig. 5. Hence, it follows immediately that a net repulsion occurs when the ABPs are predominantly depleted from or saturated within the inclusions.

The signs of the internal and external forces depend on the distribution of ABPs interacting with the enclosing membranes of the inclusions in their interior and exterior regions. Based on our simulation results for the ABP distributions and the resulting force components, we can divide the (Pe_m, Pe_c) plane to three parametric regions I-III, as shown in Fig. 9. The boundary lines here are determined by numerical interpolation of data obtained by fixing Pe_c (Pe_m) and scanning the Pe_m (Pe_c) axis at the resolution of $\Delta Pe_m = 5$ ($\Delta Pe_c = 5$). In all of these three parametric regions, ABPs are more strongly concentrated at the narrow and wedge-shaped exterior region, intervening the two inclusions, where ABP trapping effects are predominant. This is the primary source of the all-repulsive external component of the force F_0^{ext} . However, as schematically shown in Fig. 10, in region I, the ABPs that are found within the inclusions show stronger steric overlaps with the enclosing membranes at the distal parts of the interior region (the ABPs found

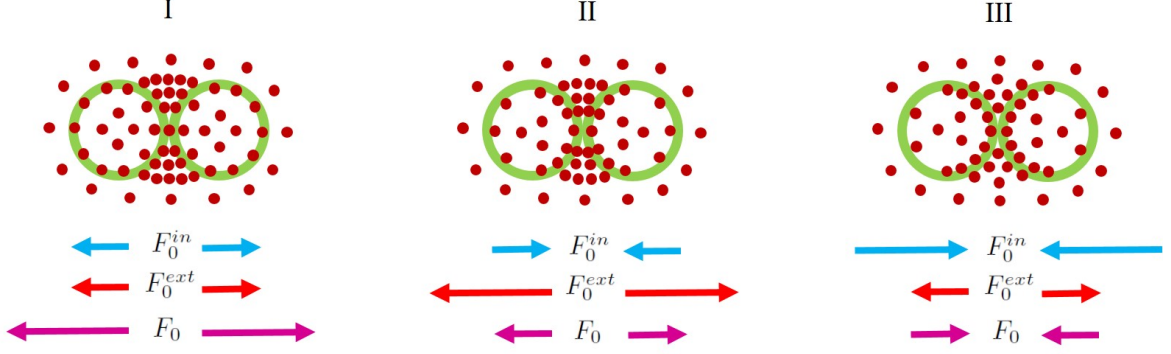


Figure 10. Schematic views of the parametric regions I-III as determined in Fig. 9 and explained in the text. Because of the preferred spatial distribution of ABPs, the external component of the force acting on the inclusions remains always repulsive, while the internal force can become repulsive (I) or attractive (II, III). The interplay between the magnitudes of these force components leads to overall repulsion (I, II) or attraction (III).

at the proximity of the intervening wedge-shaped gap between the inclusions show weaker steric overlaps with the enclosing membranes mainly because the inside ABPs also experience stronger inward-pointing repulsions from the outside ABPs that are accumulated in the outside inter-inclusion gap). As such, the inside ABPs tend to push the inclusions apart, making the internal force, F_0^{in} , repulsive as well. Region I thus corresponds to the situation, where F_0^{in}, F_0^{ext} and $F_0 > 0$. In regions II and III, the ABPs that are found within the inclusions are more strongly concentrated at the proximity of the inter-inclusion gap and induce an attractive internal force. In region II, because of low concentration or low motility of ABPs inside the inclusions, such an attractive internal force cannot dominate the repulsive force due to external ABPs and, as a result, the total effective force turns out to be repulsive. This region corresponds to the situation, where $F_0^{in} < 0$, $F_0^{ext} > 0$ (that is, $|F_0^{in}| < |F_0^{ext}|$) and $F_0 > 0$. In region III, the inside ABPs acquire sufficient concentration and motility to induce attractive internal force to dominate the repulsive external force. This region corresponds to the situation, where the internal area fraction takes intermediate values, approximately in the range of 0.1 – 0.5 (see Fig. 5). In region III, $F_0^{in} < 0$, $F_0^{ext} > 0$ (with $|F_0^{in}| > |F_0^{ext}|$) and $F_0 < 0$.

D. Role of inclusion size and ABP area fraction

The general behavior of the force profiles with the surface-to-surface separation of the inclusions remains the same as the inclusion size is increased; see Fig. 11 (top). The larger the inclusion size the larger will be the magnitude and the range of the force experienced from the ABPs. This is expected because the increased perimeter of the enclosing membrane of the inclusions and also its reduced curvature lead to larger residence times for the ABPs near the inclusions and, hence, larger proximal ABP concentrations [32]. It turns out that the

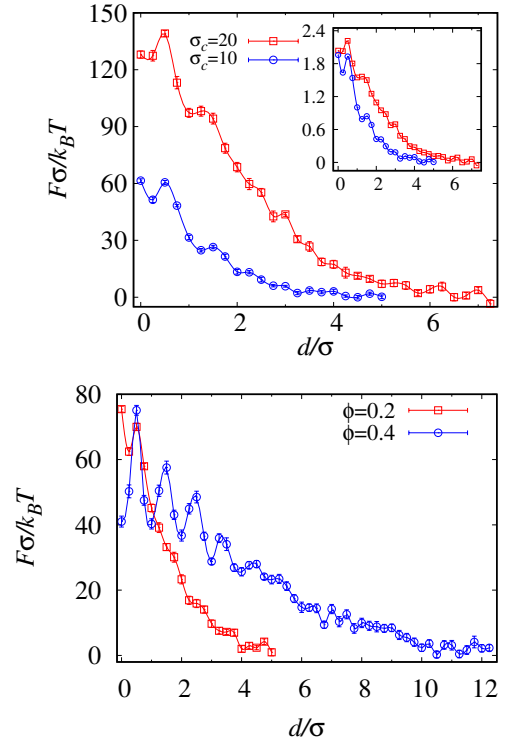


Figure 11. Top: Effective force acting on the inclusions as a function of their rescaled surface-to-surface distance, d/σ , for two different sizes of the inclusions $\sigma_c = 5$ and 10 at fixed overall area fraction of ABPs in the system, $\phi = 0.2$, and area fraction of inclusions, $\phi_c = 0.05$. The inset shows the force divided by the perimeter of the inclusions as a function of their rescaled surface-to-surface distance. Bottom: The same quantity plotted for two different overall area fractions of ABPs in the system $\phi = 0.2$ and 0.4 at fixed area fraction of inclusions, $\phi_c = 0.025$. In both panels, we have fixed $Pe_c = 0$ and $Pe_m = 20$.

magnitude of the effective force divided by the perime-

ter of inclusions grows with the inclusion size as shown in the inset of Fig. 11 (top). In the calculation of the effective force for larger inclusions, we resize the simulation box proportionally with the size of the inclusions to enable comparison of the effective force at fixed inclusion area fraction, $\phi_c = 0.05$, as the force depends on this parameter as well.

In systems with larger area fractions, a relatively larger fraction of ABPs accumulate inside and around the inclusions, which in effect leads to a larger and longer-ranged force profile as shown Fig. 11 (bottom). In this case, there will be a larger number of ABP rings formed around the inclusions as reflected by the larger number of peaks seen in the force profiles.

V. CONCLUSION

We have used extensive Brownian Dynamics simulations to study the behavior of self-propelled, active Brownian particles (ABPs) in a bath containing two permeable inclusions. The inclusions consist of permeable enclosing membranes defined by a soft potential barrier. Such a construction enables us to explore the effects of mismatching motility strengths for the ABPs in the interior and exterior regions of the inclusions and, thereby, the spatial distribution of ABPs and the effective forces imparted on the inclusions as the ABPs interact with or pass through their enclosing membranes. The ABPs form ringlike structures inside and outside the inclusions, but these vary with the interior/exterior motility strengths. For instance, such structures are prominent in regions outside (inside) the inclusions, when the exterior (interior) motility strength is sufficiently small and the ABPs are mainly found outside (inside) the inclusions. In such cases, we find repulsive effective forces acting on the inclusions. Such repulsive forces have previously been reported in the case of impenetrable inclusions immersed in an active bath [14, 15]. In the case of permeable inclusions, however, the effective forces can be repulsive or attractive, depending on the strengths of the interior/exterior Péclet numbers. We have shown that the behavior of the effective force can be understood by decomposing it to external and internal components; while the external force turns out to be repulsive, the internal force is found to be repulsive below a certain threshold Pe_c (this region being approximately where the internal ABP concentration is saturated) and it is found to be attractive above the said threshold. Our results indicate that attractive effective forces originate from the internal force component. Effective force is mostly repulsive when the concentration of ABPs inside the inclusions is either nearly fully diluted or saturated. In the diluted case, the external force makes the major contribution to the effective force, making it repulsive. In the saturated case, the internal ABPs are strongly packed within the inclusions and form a steric ‘bridge’ that helps transfer the swim pressure of the outside to the inside regions. External ABPs that accumulate in the intervening gap between

the inclusions push the internal ABPs away toward the distal regions of the interior of the inclusions, inducing a repulsive internal force and, thereby, a repulsive effective force. When the internal ABP concentration is not saturated, there is no such force transfer effect and the internal force is attractive. In the intermediate case, the internal force is typically greater than the external force, producing an attractive net force. We also find oscillatory behaviors for the force-distance profiles, which is intensified and becomes longer-ranged, as the ABP area fraction is increased, due to the more strong layering of ABPs in and around the inclusions.

Inter-colloidal forces play a crucial role in determining physical properties of colloidal suspensions such as their macroscopic phases (see Ref. [1] and references therein). Our investigation thus shows that active fluids can mediate both repulsive and attractive forces (with dynamically controlled range and magnitude) between permeable inclusions and, as such, would be expected to engender nontrivial phase behaviors in a (nonequilibrium) suspension of such inclusions. In sufficiently dense suspensions, many-body effects may also come into play. A few recent studies have considered the role of two- and many-body interactions between hard inclusions in an active fluid [14–26]. It is interesting to generalize these studies to the case of permeable inclusions and active droplets [46–48], going beyond the study presented here. Other possible extensions of our study include modeling the deformability of the enclosing membranes, mobility of the inclusions, and the shape and nonsteric (e.g., hydrodynamic and aligning) interactions of active particles.

VI. CONFLICTS OF INTEREST

There are no conflicts of interest to declare.

VII. ACKNOWLEDGEMENTS

A.N. acknowledges partial support from the Associateship Scheme of The Abdus Salam International Centre for Theoretical Physics (Trieste, Italy). M.S. thanks M. Zarif for useful discussions. We thank S. Abbasi for reviewing the manuscript. We thank the High Performance Computing Center (School of Computer Science, IPM) for computational resources.

VIII. AUTHOR CONTRIBUTIONS

M.S. developed the numerical model, performed the simulations, generated the output data and the figures, and analyzed the results. Both authors contributed to the discussions and development of the key concepts presented herein, and reviewed the manuscript. A.N. conceived the study and supervised the research.

-
- [1] H. Lekkerkerker and R. Tuinier, *Colloids and the Depletion Interaction* (Springer Netherlands, 2011).
 - [2] C. N. Likos, *Phys. Rep.* 348, 267 (2001).
 - [3] J. N. Israelachvili, *Intermolecular and Surface Forces* 3rd edition (Academic Press, London, 2011).
 - [4] S. Asakura and F. Oosawa, *J. Chem. Phys.* 22, 1255 (1954).
 - [5] S. Asakura and F. Oosawa, *J. Polym. Sci.* 33, 183 (1958).
 - [6] C. Bechinger, R. Di Leonardo, H. Löwen, C. Reichhardt, G. Volpe, and G. Volpe, *Rev. Mod. Phys.* 88, 045006 (2016).
 - [7] J. Elgeti, R. G. Winkler and G. Gompper, *Rep. Prog. Phys.* 78, 056601 (2015).
 - [8] A. Zttl and H. Stark, *J. Phys.: Cond. Matt.* 28, 253001 (2016).
 - [9] P. Romanczuk, M. Bar, W. Ebeling, B. Lindner, and L. Schimansky-Geier, *Eur. Phys. J. Special Topics* 202 1 (2012).
 - [10] A. M. Menzel, *Phys. Rep.* 554, 1 (2015).
 - [11] M. Br, R. Gromann, S. Heidenreich, and F. Peruani, *Annu. Rev. Condens. Matter Phys.* 031119, 050611 (2019).
 - [12] M. C. Marchetti, J. F. Joanny, S. Ramaswamy, T. B. Liverpool, M. R. J. Prost, and R. A. Simha, *Rev. Mod. Phys.* 85, 1143 (2013).
 - [13] S. Ramaswamy, *Annu. Rev. Condens. Matter Phys.* 1, 323 (2010).
 - [14] J. Harder, S. A. Mallory, C. Tung, C. Valeriani and A. Cacciuto, *J. Chem. Phys.* 141, 194901 (2014).
 - [15] M. Z. Yamchi and A. Naji, *J. Chem. Phys.* 147, 194901 (2017).
 - [16] F. Smallenburg and H. Löwen, *Phys. Rev. E* 92 (3), 032304 (2015).
 - [17] R. Ni, M. A. Cohen Stuart, and P. G. Bolhuis, *Phys. Rev. Lett.* 114, 018302 (2015).
 - [18] S. A. Mallory, A. Saric, C. Valeriani, and A. Cacciuto, *Phys. Rev. E* 89, 052303 (2014).
 - [19] L. Angelani, C. Maggi, M. L. Bernardini, A. Rizzo, and R. Di Leonardo, *Phys. Rev. Lett.* 107, 138302 (2011).
 - [20] D. Ray, C. Reichhardt, and C. Olson Reichhardt, *Phys. Rev. E* 90, 013019 (2014).
 - [21] L. R. Leite, D. Lucena, F. Q. Potiguar, and W. P. Ferreira, *Phys. Rev. E* 94, 062602 (2016).
 - [22] E. F. Semeraro, J. M. Devos, and T. Narayanan, *J. Chem. Phys.* 148, 204905 (2018).
 - [23] Y. Hua, K. Li, X. Zhou, L. He, and L. Zhang, *Soft Matter* 14, 5205 (2018).
 - [24] J. Codina, and I. Pagonabarraga, *J. Chem. Phys.* 151 (16), 164903 (2019).
 - [25] Y. Baek, A. P. Solon, X. Xu, N. Nikola, and Y. Kafri, *Phys. Rev. Lett.* 120, 058002 (2018).
 - [26] P. Dolai, A. Simha, and S. Mishra, *Soft Matter* 14, 6137-6145 (2018).
 - [27] H. H. Wensink, and H. Löwen, *Phys. Rev. E* 78, 031409 (2008).
 - [28] J. Elgeti, and G. Gompper, *Europhys. Lett.* 85, 38002 (2009).
 - [29] J. Elgeti, and G. Gompper, *Europhys. Lett.* 101, 48003 (2013).
 - [30] A. Wysocki, J. Elgeti, and G. Gompper, *Phys. Rev. E* 91, 050302 (2015).
 - [31] G. Volpe, I. Buttinoni, D. Vogt, H.-J. Kmmerner, and C. Bechinger, *Soft Matter* 7, 88108815 (2011).
 - [32] S. A. Mallory, C. Valeriani, and A. Cacciuto, *Phys. Rev. E* 90, 032309 (2014).
 - [33] M. J. Schnitzer, S. M. Block, H. C. Berg, and E. M. Purcell, *Symp. Soc. Gen. Microbiol.* 46, 15 (1990).
 - [34] M. J. Schnitzer, *Phys. Rev. E* 48, 2553 (1993).
 - [35] M. P. Magiera and L. Brendel, *Phys. Rev. E* 92, 012304 (2015).
 - [36] C. Lozano, B. ten Hagen, H. Löwen, and C. Bechinger, *Nat. Commun.* 7, 12828 (2016).
 - [37] J. Grauer, H. Löwen, and L. M. Janssen, *Phys. Rev. E* 97, 022608 (2018).
 - [38] J. Stenhammar, R. Wittkowski, D. Marenduzzo, and, M. E. Cates, *Sci. Adv.* 2, e1501850 (2016).
 - [39] A. Sharma and J. M. Brader, *Phys. Rev. E* 96, 032604 (2017).
 - [40] S. Jahanshahi, C. Lozano, B. ten Hagen, C. Bechinger, and H. Löwen, *J. Chem. Phys.* 150, 114902 (2019).
 - [41] H. D. Vuijk, A. Sharma, D. Mondal, J. Sommer, and H. Merlitz, *Phys. Rev. E* 97, 042612 (2018).
 - [42] A. Callegari, G. Volpe, *Numerical Simulations of Active Brownian Particles*. In: Toschi F., Sega M. (eds) *Flowing Matter. Soft and Biological Matter*. Springer, Cham (2019).
 - [43] R. W. Baker, *Membrane Technology and Applications* 3rd edition (Wiley, USA, 2012).
 - [44] S. A. Safran, *statistical thermodynamics of surfaces interfaces and membranes* (Addison-Wesley, USA, 1994).
 - [45] K. Larsson, P. Quinn, K. Sato and F. Tiberg, *Lipids: Structure, physical properties and functionality* (Elsevier Science, 2006).
 - [46] D. Zwicker, R. Seyboldt, C. A. Weber, A. A. Hyman, and F. Jülicher, *Nat. Phys.* 13, 408 (2017).
 - [47] T. Jamali and A. Naji, *Soft Matter* 14, 4820 (2018).
 - [48] E. Tjhung, C. Nardini, and M. E. Cates, *Phys. Rev. X* 8, 031080 (2018).
 - [49] J. Happel and H. Brenner, *Low Reynolds Number Hydrodynamics: with special applications to particulate media* (Springer Netherlands & Martinus Nijho Publishers, The Hague, The Netherlands, 1983).
 - [50] M. Abkenar, K. Marx, T. Auth, and G. Gompper, *Phys. Rev. E* 88, 062314 (2013).
 - [51] G. S. Redner, M. F. Hagan, and A. Baskaran, *Phys. Rev. Lett.* 110, 055701 (2013).